In Situ Alloying of Ti-6Al-7Nb with Copper Using Laser Powder Bed Fusion

Paul Steinmeier * , Kay-Peter Hoyer , Nelson Filipe Lopes Dias , Reiner Zielke , Wolfgang Tillmann , Mirko Schaper

Posted Date: 26 November 2025

doi: 10.20944/preprints202511.1915.v1

Keywords: titanium alloys; Ti-6Al-7Nb; copper addition; additive manufacturing; laser powder bed fusion; microstructure; mechanical properties; biomaterials

 doi:10.20944/preprints202511.1915.v1

Article

In Situ Alloying of Ti-6Al-7Nb with Copper Using Laser Powder Bed Fusion

Paul Steinmeier [1,2,*], Kay-Peter Hoyer [1,2], Nelson Filipe Lopes Dias [3], Reiner Zielke [3], Wolfgang Tillmann [3] and Mirko Schaper [1,2]

[1] Chair of Materials Science (LWK), Paderborn University, Warburger Straße 100, 33098 Paderborn, Germany
[2] Institute for Lightweight Design with Hybrid Systems (ILH), Paderborn University, Mersinweg 7, 33100 Paderborn, Germany
[3] Institute of Materials Engineering, TU Dortmund University, Leonhard-Euler-Straße 2, 44227 Dortmund, Germany
* Correspondence: steinmeier@lwk.uni-paderborn.de

Abstract

Titanium alloys are widely employed for biomedical implants due to their favourable combination of strength, corrosion resistance, and biocompatibility. A drawback, however, is the lack of intrinsic antibacterial functionality. In this study, Ti-6Al-7Nb was modified with varying copper (Cu) contents (1 wt.% – 9 wt.%) via in situ alloying during metal based laser powder bed fusion (PBF-LB/M) to investigate the processing behaviour, microstructural evolution, and mechanical properties. Powder mixtures were processed under systematically varied laser parameters, with densification, surface quality, and microstructure assessed by microscopy and X-ray diffraction, while hardness and tensile properties were characterised through mechanical testing. The results demonstrate that dense samples (> 99.9 %) can be achieved for all investigated copper amounts, although the homogeneity is strongly dependent on the process parameters. An increasing copper content promotes β-phase stabilisation, Ti_2Cu precipitation, and significant grain refinement with a transition from columnar to equiaxed structures. Hardness and yield strength increase nearly linearly with increasing copper content, while the ductility decreases sharply at ≥ 5 wt.% Cu due to intermetallic formation, hot cracking, and brittle fracture mechanisms. These findings highlight both the potential and the limitations of copper additions in Ti-6Al-7Nb processed by PBF-LB/M. Overall, moderate additions of 1 wt.% – 3 wt.% Cu appear most promising, offering improved mechanical performance while preserving sufficient ductility and manufacturability for biomedical applications.

Keywords: titanium alloys; Ti-6Al-7Nb; copper addition; additive manufacturing; laser powder bed fusion; microstructure; mechanical properties; biomaterials

1. Introduction

Titanium-based alloys have become a popular choice as metallic biomaterials for load-bearing implants due to their favourable properties, including high biocompatibility, high specific strength, a low Young's modulus compared to steel or CoCr alloys, and excellent corrosion resistance [1,2]. Developed as an alternative to the widely used Ti-6Al-4V alloy, Ti-6Al-7Nb substitutes vanadium (V) with niobium (Nb), thereby avoiding the potential cytotoxic effects associated with vanadium [3–5]. As a result, Ti-6Al-7Nb has been adopted in orthopaedic and dental implantology owing to its excellent biocompatibility and mechanical properties [6–8].

However, a significant drawback of most titanium-based alloys is their lack of intrinsic antibacterial functionality, which permits the formation of biofilms. This issue is reflected in the high prevalence of implant-associated infections, frequently caused by organisms such as Staphylococcus aureus and Escherichia coli. As infection can compromise implant integration and longevity, often

 doi:10.20944/preprints202511.1915.v1

necessitating revision surgery, this represents a major limitation in the use of titanium alloys for permanent implants [9,10].

To address this limitation, there has been an increasing focus on the use of antibacterial elements such as silver, zinc, or copper either as surface coatings or through alloying. [11]. Among these, copper is particularly notable due to its effective antibacterial activity and low cytotoxicity at low concentrations [12–14]. Both in-vitro and in-vivo studies have shown that copper-bearing titanium alloys exhibit strong antibacterial properties without compromising cytocompatibility, provided the copper content is appropriately controlled [15–17]. Systematic investigations on binary Ti–Cu alloys have demonstrated enhanced bacterial inhibition with increasing copper content. However, excessive copper additions can negatively impact mechanical and corrosion properties, whereas moderate amounts may also provide benefits such as solid-solution strengthening and precipitation hardening [12,18–20]. There is growing evidence that moderate copper additions attain a favourable balance between antibacterial efficacy while maintaining or even improving the alloy's overall performance [16,21].

Despite numerous scientific studies on titanium–copper-based alloys, the fundamental understanding of titanium's interaction with copper remains incomplete. Studies performed by Williams et al. have shown that the presence of 8 wt.% copper was insufficient to retain the β phase in quenched samples, suggesting an athermal, diffusionless transformation to Ti_2Cu [22]. In a recent study, Donthula et al. found evidence for both a sluggish and eutectoid transformation taking place in a hypereutectoid Ti-Cu alloy [23]. Furthermore, Dobromyslov and Kazantseva reported that at a sufficiently high copper concentration and cooling rate, the stabilisation of metastable β at room temperature is possible. They reported that at 13 at.% (16.5 wt.%) copper and a cooling rate of more than 1000 K/s, the microstructure after quenching consists almost entirely of retained β, with only minor traces of α [24]. Additionally, Dobromyslov investigated the temperature-dependent precipitation rate of Ti_2Cu, detecting this phase after 10 seconds at around 700 °C and identifying copper as the fastest-precipitating d-metal in titanium in the case of binary alloy systems [25]. Looking into the complex character of copper as a β-stabilizer in ternary alloys, investigations performed by Takahashi et al. on air-cooled Ti-xNb-yCu samples revealed an α+β microstructure for Ti-8Nb-2Cu, but a mixture of α + Ti_2Cu for Ti-10Nb-5Cu despite containing a higher content of β-stabilizing elements than the former alloys [26]. Zhao et al. examined water-cooled samples of Ti-10Nb-3Cu, Ti-30Nb, and Ti-30Nb-3Cu, finding an α+β microstructure for Ti-10Nb-3Cu and suppression of α formation in Ti30Nb by adding 3 wt.% copper, resulting in a pure β microstructure [27]. Similar findings were reported by Li et al. with a transition from β+α" in Ti-35Nb to β in Ti-35Nb-2Cu, which accounted for a reduction of the martensitic starting temperature [28]. Taking all these results into account, it is evident that the β-stabilizing character of Cu is highly sensitive to both cooling rate and alloy composition.

Recent advances in additive manufacturing, particularly powder bed fusion with laser beam (PBF-LB/M), have created new possibilities for the in-situ alloying of Ti-6Al-7Nb with copper directly during near-net shape manufacturing [29,30]. This approach allows fabricating patient-specific implants with precisely controlled surface chemistry and tailored microstructures to address clinical requirements [30,31]. However, achieving a homogeneous copper distribution and defect-free microstructures requires careful optimisation of process parameters such as laser power, scanning speed, and hatch distance [20,32,33]. Variations in these parameters influence the thermal history, thereby affecting phase formation, grain size, and ultimately both mechanical and biological performance [34–37]. Consequently, the design of antibacterial Ti-6Al-7Nb-xCu alloys via PBF-LB/M remains a complex challenge, necessitating a comprehensive investigation into the relationships between processing, microstructure, and properties.

Despite the potential advantages of copper addition to the Ti-6Al-7Nb system and the opportunities offered by in-situ alloying via PBF-LB/M, research in this area remains limited. Most existing studies have addressed conventional fabrication routes or binary titanium-copper alloys, while comprehensive investigations of multi-component systems produced by advanced additive

 doi:10.20944/preprints202511.1915.v1

manufacturing techniques are still limited [38,39]. A thorough understanding of the effects of process parameters on the microstructure and densification of additively manufactured Ti-6Al-7Nb-Cu alloys is, therefore, essential for optimising their fabrication and broadening their application in biomedical implants.

In this work, we present a systematic study of laser powder bed fusion processing and its influence on the microstructure and mechanical properties of Ti-6Al-7Nb alloys with varying copper contents (1 wt.%, 3 wt.%, 5 wt.%, 7 wt.%, and 9 wt.%). Comprehensive microstructural characterisation is carried out to address the relationships between processing conditions, structural evolution, and mechanical response, thereby providing a foundation for process optimisation and the future development of advanced titanium-based biomaterials.

2. Materials and Methods

2.1. Powder Mixing and Characterisation

The powders applicated in this study were prepared by mechanically mixing gas-atomised copper and Ti-6Al-7Nb (Ti67) powders (Eckart TLS GmbH, Bitterfeld, Germany) using a modified drum mixer. To minimise potential effects from powder segregation and moisture uptake, mixing was performed immediately before the PBF-LB/M process, following vacuum drying (to a relative humidity < 5 %) and under a reduced atmosphere (< 10 mPa). Powder mixtures with defined copper contents were produced, resulting in compositions of Ti-6Al-7Nb+xCu with x = 1.0 wt.%, 3.0 wt.%, 5.0 wt.%, 7.1 wt.%, and 9.0 wt.%, which are referred to as "xCu" in this study.

To characterise the pure and mixed powders, particle size distributions (PSD) were determined by laser diffraction analysis (LDA) using a Mastersizer 2000 (Malvern Panalytical GmbH, Kassel, Germany). In addition, the flowability was assessed with an RST-XS.s ring shear tester (Dr. Dietmar Schulze GmbH, Wolfenbüttel, Germany), and the powder morphology was examined by scanning electron microscopy (SEM) using a ZEISS NEON® 40. The measured particle size distribution and flowability of the powders are depicted in Figure 1.

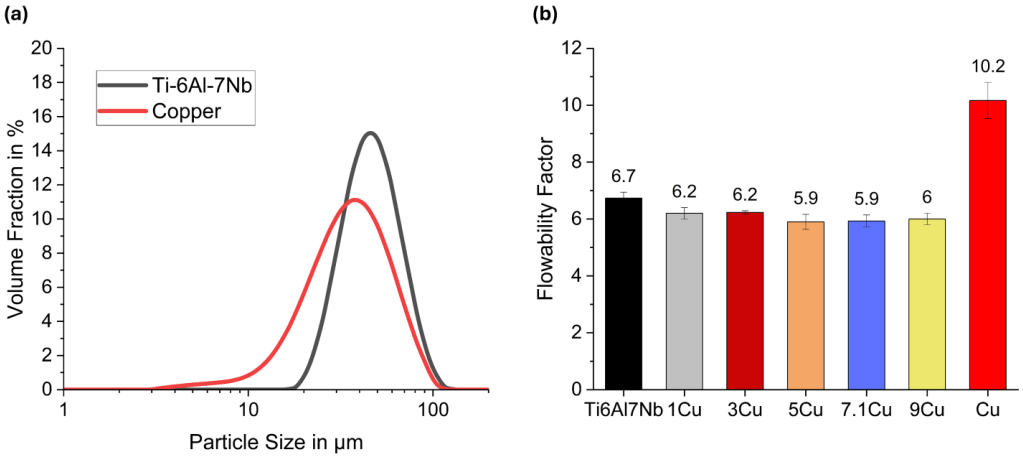

Figure 1. (a) Particle size distribution and **(b)** Flowability Factor of Ti-6Al-7Nb, the mechanically mixed powders and pure copper.

To evaluate the influence of copper addition on processability via laser powder bed fusion (PBF-LB/M), a parameter adoption was conducted using a LASERTEC 12 SLM system (DMG MORI AG, Bielefeld, Germany). All samples were fabricated on a preheated Ti-6Al-4V build platform maintained at a constant temperature of 200 °C in an inert argon atmosphere (O_2 content < 0.15 %). As part of the exposure strategy, each layer was scanned once using a 10 mm stripe pattern, with a layer-by-layer rotation of the scan direction by 61°. The layer thickness was consistently set to 50 µm, while the process parameters (laser power, scanning speed, and hatch distance) were systematically

 doi:10.20944/preprints202511.1915.v1

varied. The parameter selection was based on a central composite design (CCD), with the centre point derived from previous studies on Ti-6Al-7Nb [40]. The parameter study aimed to identify the optimal parameter combination for each powder mixture that enables the fabrication of bulk material with a porosity < 0.05 % in cube samples with dimensions of (10 × 5 × 5) mm³, as specified in Table 1.

Table 1. Adjusted processing parameters for the production of dense samples from Ti-6Al-7Nb and copper-modified powders.

Hatch Distance in µm	Scanning Speed in m/s	Laser Power in W	Modification
90	1.5	275	Ti-6Al-7Nb
			1Cu
			3Cu
80	1.25	350	5Cu
			7Cu
			9Cu

After processing the different blends, all samples were prepared metallographically by grinding and polishing up to a final stage of 50 nm colloidal silica suspension. Porosity analysis was then performed using a Keyence VHX-5000 (KEYENCE DEUTSCHLAND GmbH, Neu-Isenburg, Germany) digital microscope to determine the optimal parameters for achieving high densities.
In a subsequent parameter adaptation aimed at minimising the surface roughness, the previously determined bulk parameters were evaluated for all powder mixtures. While the hatch parameters were kept constant within each powder mixture, the contour parameters - specifically laser power and scanning speed - were varied analogously to the initial study. Following processing, the as-built surfaces were analysed at three different locations on each sample to obtain an average roughness value for each parameter set. The measured R_a values ranged from a minimum value of 8.6 µm in 1Cu to 19.6 µm in 9Cu. Since this increase was mainly attributed to a copper-rich layer forming on the surface, nearly independent of the processing parameters, no further optimisation on surface roughness was performed.

For mechanical characterisation, Vickers hardness tests (HV5) were carried out on polished cubes of (10 × 5 × 5) mm³ produced from each powder mixture, using a semi-automatic hardness tester (KB 30 FA, KB Prüftechnik GmbH, Hochdorf-Assenheim, Germany). In addition, tensile specimens were manufactured according to the geometry shown in Figure 6c), employing the process parameters identified in the preceding parameter studies. To minimise both thermal and mechanical effects, separation of the specimens from the build platform was achieved using electric discharge machining. To remove residual adhering powder, all tensile specimens were blasted with glass beads (grain size 100 µm to 200 µm), using an SMG 25 DUO (MHG Strahlanlagen GmbH) at a pressure of 4 bar. Tensile tests were performed using an MTS 858 table system equipped with a 20 kN load cell and an MTS Modell 632.29F-30 extensometer (MTS Systems Corporation, Eden Prairie, MN, USA), under displacement control at a cross-head speed of 1.5 mm/min, following DIN EN ISO 6892-1. All tensile tests were conducted at room temperature, with the loading direction aligned parallel to the build (z) axis on dog-bone specimens with a necking radius of 2 mm.

For the thermodynamic investigation, equilibrium phase diagrams for various compositions of Ti-6Al-7Nb+xCu were calculated using the Calculation of Phase Diagrams (CALPHAD) approach, employing a database specifically developed for Ti-based multicomponent systems (TCTI6). The crystalline phases were analysed by X-ray diffraction (XRD; D8 Advance, Bruker, Madison, WI, USA), using copper K_α radiation (λ = 0.154187 nm) at an operating current of 40 mA and a voltage of 40 kV, over a 2θ range of 20° to 120°, with a step size of 0.035° and an exposure time of 1 s.

To investigate the influence of copper on the as-built microstructure, light optical microscopy (LOM) was performed after etching with Kroll's reagent for general microstructural analysis, and with a solution of KOH and H_2O_2 for the determination of prior β grain size. In addition, using a Zeiss Ultra Plus (Carl Zeiss AG, Oberkochen, Germany) scanning electron microscopy and energy-

 doi:10.20944/preprints202511.1915.v1

dispersive X-ray spectroscopy (EDS) were conducted on both polished and Kroll's reagent-etched samples to enhance the visibility of microstructural features.

3. Results

3.1. Calculated Pseudo-Binary Phase Diagram

Figure 1 shows the pseudo-binary phase diagram of Ti-6Al-7Nb+xCu, calculated via thermodynamic simulations. For ease of calculation, the aluminium and niobium contents were kept at 6 wt.% and 7 wt.%, respectively, while the copper and titanium fractions were varied. The results obtained using the TCTI6 database represent thermodynamic equilibrium and thus differ significantly from the as-built condition investigated in this study. Considering that the interactions of copper in multicomponent titanium alloys are still not fully known, supported by the fact that not all equilibrium states can be calculated, the phase diagram will be discussed in more detail in the following section.

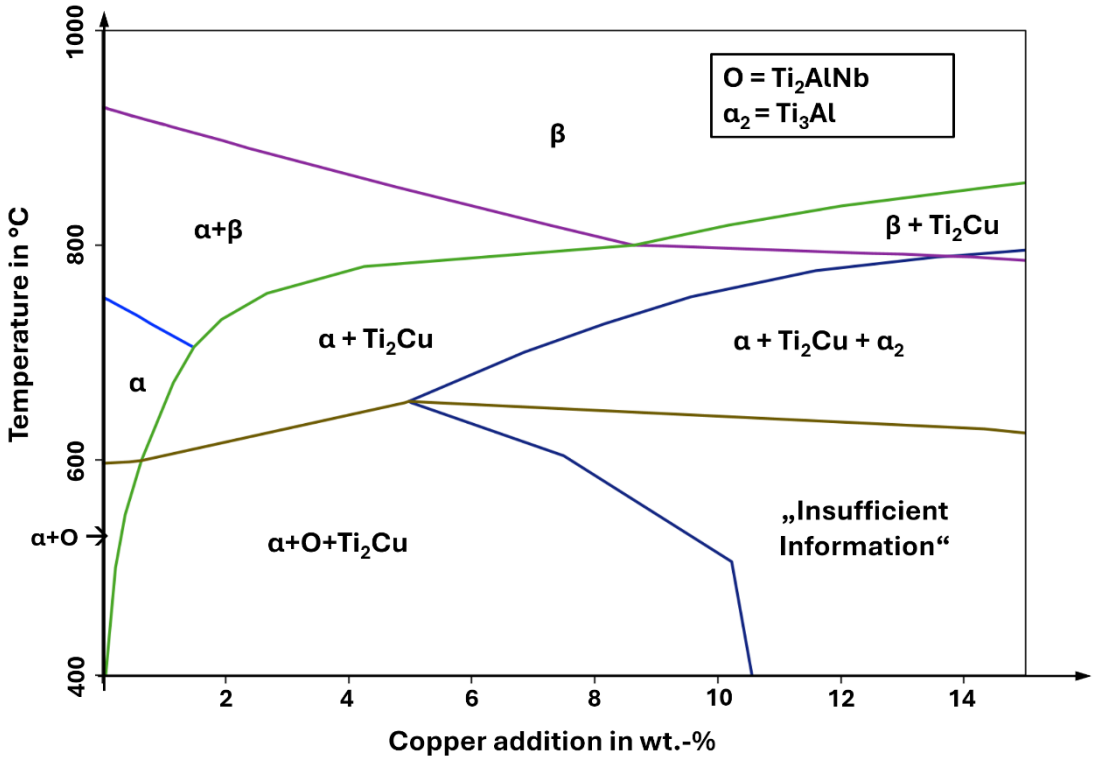

Figure 2. Pseudobinary equilibrium phase diagram for the system Ti-6Al-7Nb + Cu as a function of temperature, calculated via CALPHAD using the TCTI6 database.

At high temperatures, the calculated phase diagram predicts a behaviour very similar to the binary Ti–Cu system, characterised by a strong reduction in both the liquidus and β transus temperatures. The β-stabilising effect of copper is evident. Compared to the binary alloy, the eutectoid composition at which β transforms into α + Ti_2Cu is shifted just slightly towards higher copper content, from 7.04 wt.% to approximately 8.5 wt.%. The O-phase (ordered Ti_2AlNb) is only marginally affected by copper addition, whereas a stabilisation of the α_2 (Ti_3Al) phase is predicted at higher copper concentrations. Further calculations predict the formation of only 5 vol.% α_2 in a 10Cu alloy, but a substantial increase to over 50 vol.% in the 19Cu alloy at around 700 °C. As the applied CALPHAD approach is based on thermodynamic equilibrium, it cannot predict martensite formation. However, since martensite and other metastable phases are frequently observed in PBF-LB/M produced materials, the phase diagram will be discussed in detail later regarding possible phase formation, considering all experimental results, formation enthalpies, and kinetic effects.

 doi:10.20944/preprints202511.1915.v1

3.2. Characterisation of the As-Built Microstructures

The phase composition of the various in situ alloys was experimentally evaluated by XRD, with the results presented in Figure 3. Increasing the copper content has a significant effect on the observed phase composition. XRD analysis of the Ti67 reference sample reveals only diffraction angles typical of an α/α' microstructure, probably overall martensitic owing to the high cooling rates during PBF-LB/M. The 1Cu alloy exhibits a similar diffraction pattern, with diffraction angles nearly identical to Ti67 but with noticeable changes in the relative intensities.

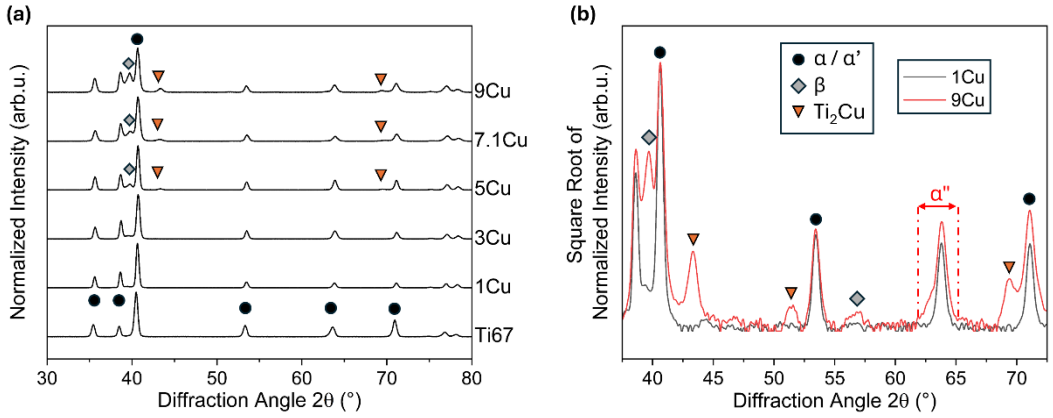

Figure 3. XRD diffractograms of Ti-6Al-7Nb+xCu samples in the as-built condition: **(a)** overview of the Ti-6Al-7Nb reference and all investigated compositions, **(b)** direct comparison of the square root of the normalised intensity of 1Cu and 9Cu.

From 1Cu onwards, in all copper-containing alloys, a slight shift of the α diffraction peaks towards higher 2θ values is observed, corresponding to a reduction in lattice parameters, indicating that the measured increase in hardness is at least partially caused by substitutional hardening because of an increase in lattice strain. Additionally, a minor elevation at 39.5° suggests the presence of β-Ti, and this diffraction feature becomes more prominent with increasing copper content. The identification of β-Ti is further supported by another peak at 56°, which is characteristic of the β phase predicted to be stable in the Ti-6Al-7Nb+xCu system according to CALPHAD. Due to their weak intensity relative to α/α', these diffraction peaks were only visible after applying non-linear scaling of the relative intensity, as illustrated in Figure 3b.

Detected at first in 5Cu and continuing with increasing copper content, diffraction angles corresponding to the intermetallic Ti_2Cu phase are visible, with their intensity progressively increasing in 7Cu and 9Cu. Moreover, increased diffraction intensity is registered around the 39.5° β-Ti diffraction angle, accompanied by a slight broadening of the α-Ti diffraction angles, resulting in the overlapping of multiple peaks.

Light optical microscopy (LOM) analysis of the phase distribution and microstructure reveals that the copper distribution is generally inhomogeneous, showing significant variations depending on the copper content. Although the process parameters identified in the parameter studies enabled the fabrication of dense samples, a consistent distribution of copper throughout the samples was not achieved. Figure 4 presents representative micrographs of 1Cu and 9Cu, each etched with either $KOH+H_2O_2$ or Kroll's reagent, thus highlighting different aspects of the microstructure. Etching with Kroll's reagent also allows a qualitative assessment of copper concentration: darker areas correspond to elevated copper content, and vice versa.

The morphology of these inhomogeneities and copper-rich regions often resembles melt pool boundaries, suggesting that most of the copper mixing took place in the liquid state. In 3Cu, a greater number of copper-rich areas is observed compared to 1Cu. However, this trend is not observed in 5Cu, for which the highest degree of mixing is qualitatively found in 7Cu. White regions visible in the Kroll-etched micrographs, such as those in Figure 4, correspond to unmolten Ti67 particles, whose

 doi:10.20944/preprints202511.1915.v1

number increases markedly with higher copper content. Near the sample surface, a nearly continuous layer of Ti67 particles embedded within a darkened matrix can be observed. Further examination of copper accumulations, both at the surface and within the bulk, reveals a high density of defects (primarily pores and fine hot cracks) associated with these copper-rich regions.

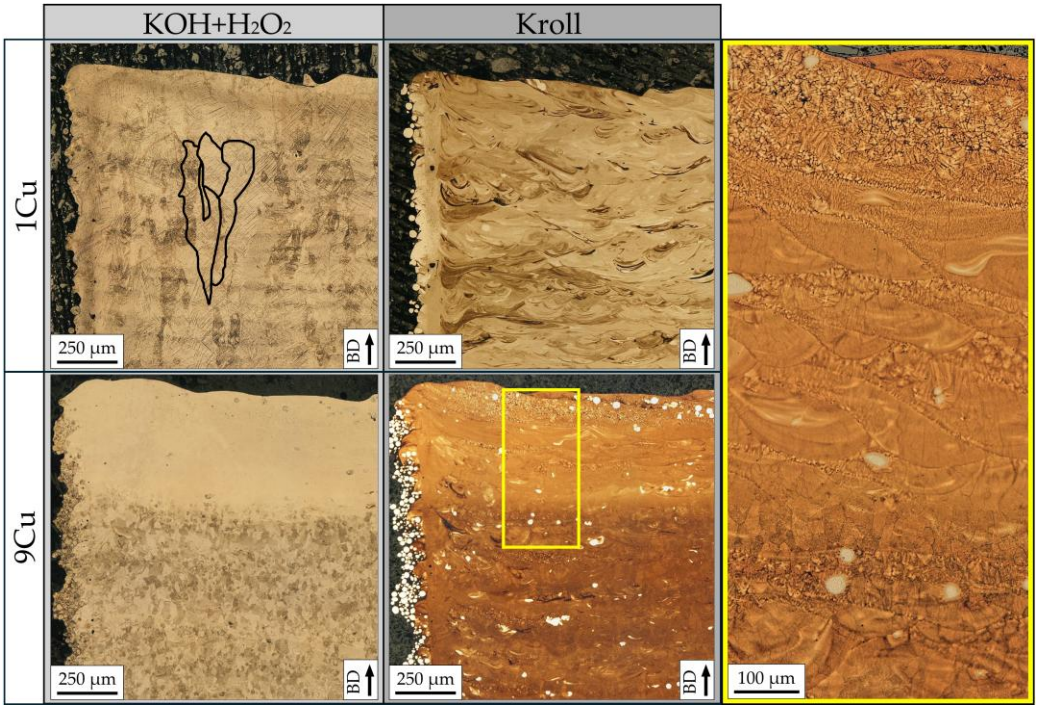

Figure 4. LOM micrographs of samples from 1Cu and 9Cu, etched with KOH+H_2O_2 and Kroll. Epitaxially grown prior β grains are marked in black in 1Cu-KOH. Shown enlarged on the right is the section outlined in yellow in 9Cu-Kroll (bottom centre) showing the fine dendritic microstructure that forms during solidification.

Apart from inhomogeneous regions resulting from inadequate mixing, the microstructure of 1Cu closely resembles that of standard Ti-6Al-7Nb produced by PBF-LB/M, featuring elongated, epitaxially grown prior β grains that are decomposed into α/α' platelets, which are often oriented at 45° to the build direction. The microstructure of 3Cu appears similar, albeit with smaller prior β grains and α/α' platelets, as well as an increased number of regions exhibiting elevated copper concentrations. Moreover, the upper ends of prior β grains (in the build direction) frequently coincide with areas of high copper content, as highlighted in Figure 4.

With increasing copper content, the reduction in prior β grain size becomes more pronounced, resulting in a transition from columnar to equiaxed grain structures. Whereas the epitaxially grown prior β grains observed in 1Cu occasionally exceed 1000 µm in the build direction, the nearly equiaxed microstructure of 5Cu consists of globular prior β grains smaller than 50 µm. An even stronger refinement occurs in 7Cu and 9Cu, where individual prior β grains are less than 10 µm in size and the grain structure exhibits clear indications of a directed solidification starting at the melt pool boundaries.

In addition to changes observed in the bulk material, notable microstructural differences are present in the uppermost, i.e. most recently in situ alloyed, layers. While no significant contrast to the bulk is apparent in 1Cu and 3Cu, the surface layers of 5Cu, 7Cu, and 9Cu show clear deviations from the bulk microstructure, with both their extent and inhomogeneity increasing with increasing copper content. As shown in detail in Figure 4, in the upper edge of a 9Cu sample etched with Kroll's reagent, a fine dendritic microstructure and darker interdendritic regions that occasionally contain unmolten Ti67 particles are present.

 doi:10.20944/preprints202511.1915.v1

Since consecutive remelting of underlying layers is critical for achieving a homogeneous distribution of copper, these uppermost layers can be interpreted as snapshots of the mixing process effectively frozen in time. The initially high cooling rates result in dendritic solidification, which gradually transitions to equiaxed grains through repeated remelting in subsequent layers. Dark-field imaging demonstrates a flat surface topology, suggesting that the features observed in bright-field images are due to differences in reflectivity rather than variations in surface relief. SEM investigations on the microstructures show that the refinement is not restricted to prior β grains but also to the size of the α/α' platelets. Shown in Figure 5 are representative SEM images of areas with homogeneous distribution of copper in 1Cu, 5Cu and 9Cu at the sample centre with regard to the building height. While 1Cu shows a microstructure consisting of α/α' platelets typical for PBF-LB/M of Ti-6Al-7Nb, a strong refinement is visible in 5Cu and 9Cu. Based on the XRD results, 5Cu presumably consists of homogeneously distributed α/α' platelets, between which small amounts of metastable β are visible. 9Cu shows an even stronger refinement but an inhomogeneous microstructure with presumably precipitates of Ti_2Cu at grain boundaries.

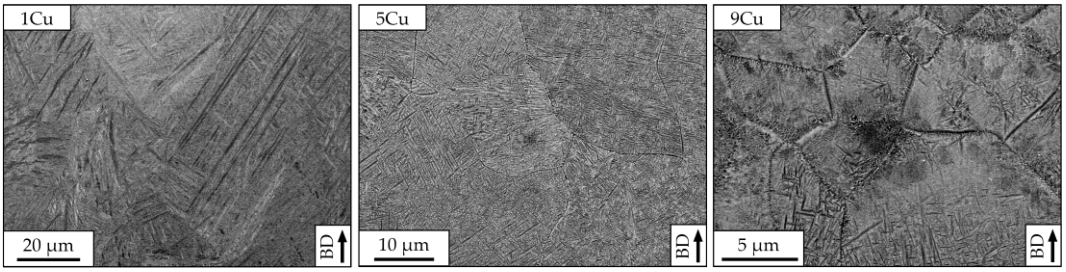

Figure 5. Representative SEM micrographs of areas with homogeneous copper distribution and the strong refinement in microstructure as visible by the change in scale.

3.2. Mechanical Properties

The results of mechanical testing demonstrate that copper addition can lead to a significant increase in both hardness and yield strength, with the payoff of a dramatically reduced elongation at break, which will be discussed in detail later. The hardness of the unmodified Ti-6Al-7Nb reference was measured at 333 ± 2 HV5, whereas the addition of 9 wt.% copper increased by approximately 60 %, reaching around 533 ± 6 HV5. The increase in hardness was found to be nearly linear, at approximately +15 HV5 per wt.% Cu. In all cases, the calculated standard deviation remained below 3 % of the respective mean value.

Tensile testing results show the strengthening effect mediated by copper on the yield stress to a certain degree for 1Cu, 3Cu and 5Cu, while failure on samples of 7Cu and 9Cu took place far below the yield strength of pure Ti-6Al-7Nb.

For illustration and ease of comparison, the most representative stress–strain curve obtained from tensile testing for each copper addition, as well as for unmodified Ti67, is presented in Figure 6. Furthermore, the copper addition exerts only a minor influence on Young's modulus, which increases from approximately 105 GPa for Ti-6Al-7Nb to a maximum of 111 GPa for 5Cu, before decreasing again for 7Cu and 9Cu.

 doi:10.20944/preprints202511.1915.v1

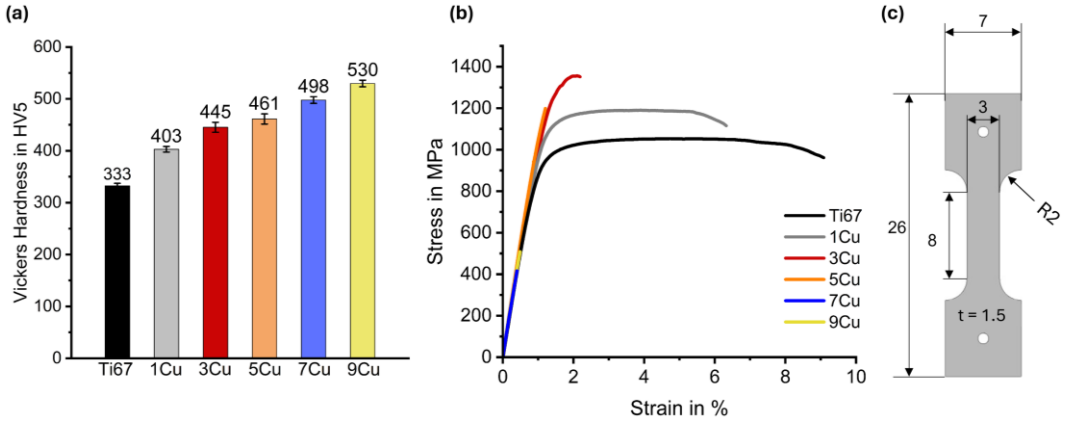

Figure 6. Results from the **(a)** hardness testing and **(b)** tensile testing of in situ alloyed Ti-6Al-7Nb+xCu samples with different copper additions performed in the as-built condition on samples with the geometry given in **(c).**

SEM analysis of the fracture surfaces was conducted to investigate the underlying causes of the reduced elongation at break, confirming that the copper addition induces a transition from ductile to brittle fracture behaviour. Fracture surfaces of samples with low copper contents are characterised by intergranular fracture along prior β grain boundaries, whereas those with higher copper content exhibit brittle fracture with transgranular features and facets oriented nearly perpendicular to the loading direction.

As shown in Figure 7, the fracture surface of the 1Cu alloy displays a high density of ductile dimples distributed across most of the surface, interspersed with various defects. Additionally, scattered across the 1Cu fracture surface are regions exhibiting solidification morphologies that lack evidence of plastic deformation and are therefore identified as solidification cracks. The incidence of hot cracking increases significantly in 3Cu and 5Cu, with deep secondary cracks also becoming apparent at the interface with the neighbouring bulk material with lower copper content.

Regarding the fracture mode, the transition from ductile to brittle occurs at 5 wt.% Cu, with both brittle and ductile features visible in the fracture surfaces of 5Cu as shown in Figure 7 b). Small dimples indicating a ductile fracture mode can be seen on prior β grains, indicating intergranular fracture right beside transgranular flat cleavage facets with a size of just a few microns. As expected from the tensile tests, the fracture surfaces of 7Cu and 9Cu exhibit no dimples or areas of plastic deformation. Occasional intercrystalline features on these samples are covered with solidification cells rich in copper, as determined via EDS. Shown in Figure 7d) is a fracture surface of 9Cu characterised by flat feathery cleavage facets with river markings, separated by cleavage steps. Further investigations of the brittle fracture surfaces via EDS reveal a general lack of niobium relative to the nominal composition and overall high concentrations of aluminium and titanium, occasionally accompanied by increased amounts of copper.

 doi:10.20944/preprints202511.1915.v1

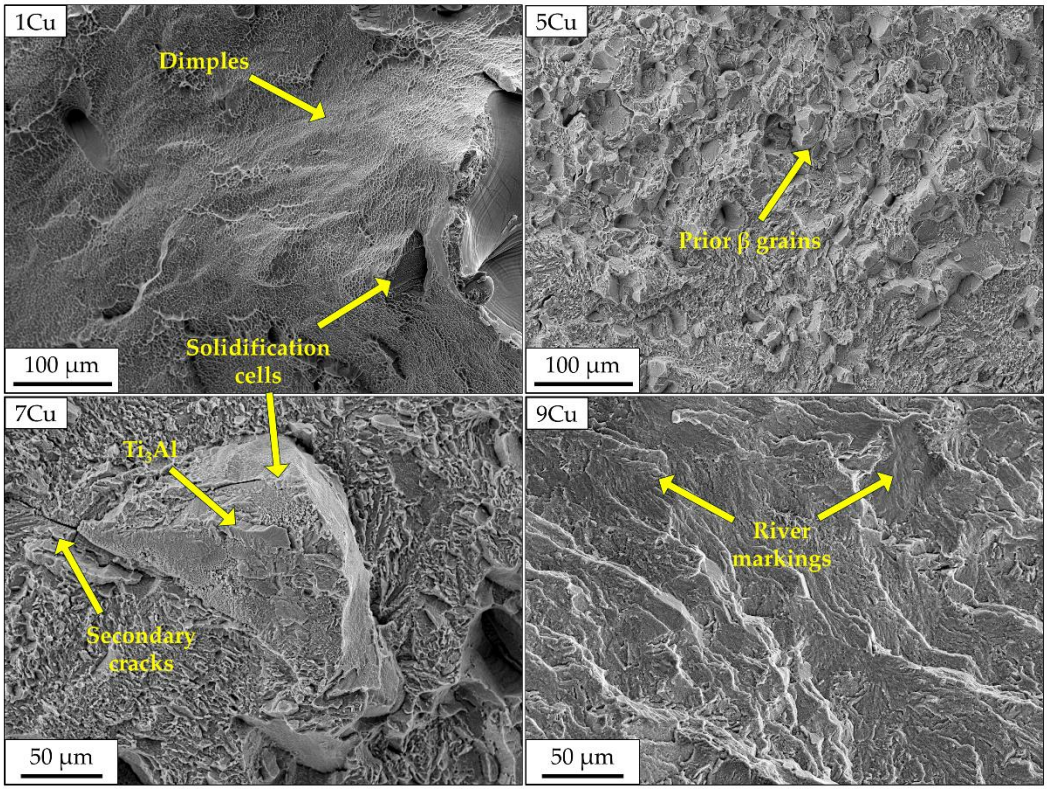

Figure 7. SEM-images of tensile fracture surfaces of Ti-6Al-7Nb+xCu with different amounts of added copper, as well as highlighted features indicating the change in fracture mode from ductile to brittle with increased copper addition.

4. Discussion

4.1. Parameter Studies and Processability

While parameter studies are generally performed to produce samples with low porosity at high build rates, in situ alloying additionally requires achieving high homogeneity, i.e., effective mixing of alloying elements. Initially, the influence of processing parameters—especially the energy density—on the degree of mixing was considered negligible, as solution annealing was assumed to be essential for obtaining a homogeneous copper distribution throughout the samples. However, subsequent investigations disproved this assumption.

Figure 8 shows samples made from 3Cu, processed with different parameters and etched with Kroll's reagent, where distinct differences in homogeneity can be observed. Further analysis revealed that energy density is indeed an important factor for effective mixing, as it correlates with the residence time in the liquid state. Since 1Cu and 3Cu were built with lower energy densities than 5Cu, 7Cu, and 9Cu, the improvement in homogeneity from 3Cu to 5Cu can be attributed to the different processing conditions. The higher energy required to produce dense samples from powders with higher copper content results from the increased specific heat capacity and higher reflectivity of copper at the laser wavelength of 1070 nm [41].

As shown in Figure 4, the degree of mixing in 1Cu differs significantly from that in 9Cu. Etched samples of 3Cu confirm that this difference arises from the higher laser power and lower scanning speed used for powders with greater copper content, leading to a larger melt pool and longer residence time. For comparison, Figure 8 presents micrographs of samples produced with processing parameters at the lower, medium, and upper ends of the volume energy density range.

 doi:10.20944/preprints202511.1915.v1

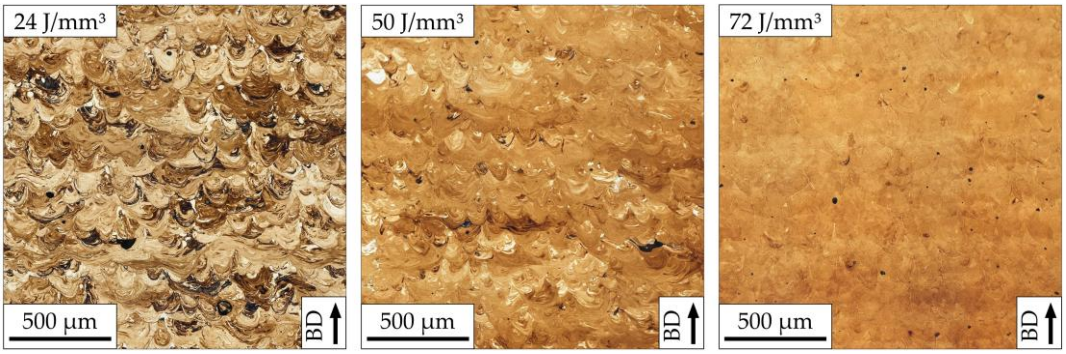

Figure 8. Micrographs of samples from Ti67+3Cu etched with Kroll manufactured with different volume energy densities. Areas of high copper concentration are coloured dark and vice versa.

Even though PBF-LB/M manufactured parts from titanium often require post-processing in the form of heat treatment to relieve residual stresses, an adjusted heat treatment that also homogenises the chemical composition after in situ alloying is both time-consuming and costly. Considering the strong interplay between chemical homogeneity and melt pool dynamics, processing mixed powders via PBF-LB/M at higher energy densities may prove more economical in terms of overall productivity, despite increasing the manufacturing time, as the need for extensive post-processing heat treatments could be drastically reduced.

Another key finding for in situ alloying of near net shaped manufacturing alloyed parts, is the formation of an outermost layer containing Ti67 particles in a copper-rich matrix on all samples, attributed to the difference in melting temperature between Ti and Cu. Since titanium and copper can form an eutectic system at ≈ 70 wt.% Cu with a melting point ≈ 700 K below the liquidus temperature of Ti67, at some distance to the melt pool, the powder bed has a temperature of $T_{Cu,\,liq} < T_{bed} < T_{Ti,liq}$. In this area, copper particles melt and envelop Ti67 particles, adhering to the outermost layer. This results in the as-built roughness being relatively independent from the used processing parameters, but instead dependent on the processed powder and the amount of copper in it. In the case of functionally graded materials, this disadvantage in terms of surface roughness and dimensional accuracy could be compensated by the advantage of targeted accumulation of the low-melting alloy partner.

4.2. Phase Evolution and Morphology

Since the CALPHAD approach can only provide an estimate of the phase composition under equilibrium conditions, differences between the as-built state and the calculated phase diagram arise from kinetic effects. While the orthorhombic O-phase (Ti_2AlNb) was predicted to account for about 20 vol% of the microstructure in equilibrium at room temperature for all investigated copper contents, no characteristic diffraction peaks were detected by XRD in the as-built condition; this absence is attributed to its relatively slow formation kinetics. Conversely, most of the copper precipitated as Ti_2Cu, as expected, owing to its extremely rapid formation kinetics and the in situ heat treatment occurring during the PBF-LB/M. Since metastable phases cannot be predicted via CALPHAD, no results concerning the extent of martensite formation or the retention of metastable β were generated. The combination of XRD and SEM investigations shows that 1Cu and 3Cu consist predominantly of α/α' in the most recently processed layers, or of an extremely fine α + β microstructure in the lower regions of the samples, also attributed to the in situ heat treatment. Subsequently, significant amounts of metastable β were detected in 5Cu, 7Cu, and 9Cu together with Ti_2Cu, leading to the conclusion that the in situ heat treatment partially promoted the decomposition into fine α + Ti_2Cu structures, with a certain amount of copper remaining in solid solution and stabilising β-Ti in conjunction with Nb. While the strong reduction of the martensite start temperature by copper, as well as its rapid diffusion and the formation of Ti_2Cu, are well established, the temperature dependence of copper's β-stabilising effect remains difficult to assess. Nevertheless,

 doi:10.20944/preprints202511.1915.v1

results from other studies [26–28] and the observation that the extent of β stabilisation, as well as the fractions of retained β and Ti_2Cu formation, depend strongly on the in situ heat treatment, suggesting that the temperature-dependent isomorphous or eutectoid character of copper is even harder to predict in ternary or higher-order titanium alloys. Supporting this approach, the broadening of peaks observed in the XRD data for 9Cu implies the beginning transition from hexagonal α′ to orthorhombic α″ martensite. Since recent investigations on binary alloys have shown that α″ martensite forms only when the atomic size difference between titanium and the alloying element is less than 9 %, a criterion met by Ti–Nb but not by Ti–Cu, this provides a starting point for further studies of martensite formation in ternary or higher-order titanium alloys.

The extent and cause of the observed refinement of prior β grains in xCu alloys depend on the copper content. In 1Cu and 3Cu, only slight refinement of prior β grains is observed, with limited inhibition of epitaxial growth evident in copper-enriched regions, most likely due to the formation of brittle intermetallic phases and their differing lattice parameters compared to β-titanium. In contrast, 5Cu, 7Cu, and 9Cu, which exhibit improved mixing as a result of the higher energy density used during processing, show not only a more homogeneous copper distribution but also significantly enhanced grain refinement and a strong columnar-to-equiaxed transition (CET). A depiction of the grain refinement observed in 9Cu is shown in Figure 9. Possible causes are heterogeneous nucleation on partially molten Ti-6Al-7Nb particles and constitutional supercooling. Scheil-Gulliver solidification simulations indicate that copper decreases the solidification temperature by approximately 500 K at 20 wt.%, leading to a strong confinement effect of β crystallites in a copper-enriched melt through constitutional supercooling (CS), ultimately inhibiting the epitaxial growth of β grains, as also proposed by Zhang et al. [42]. This theory is further supported by EDS measurements, which indicate large differences in copper content between the centres and boundaries of the refined grains, as well as a stronger refinement effect in regions with higher copper content and by LOM investigations of the uppermost layers in samples of 7Cu and 9Cu.

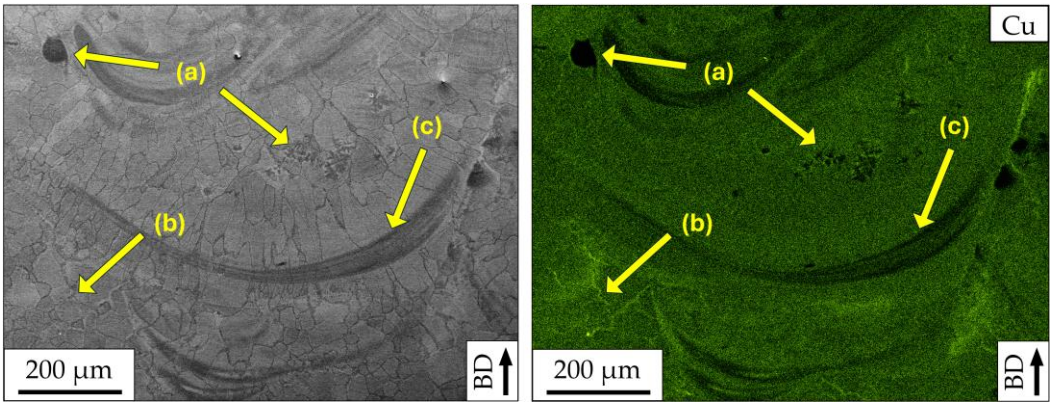

Figure 9. EDS map showing the copper distribution in Ti67+9Cu in the upper part of the sample regarding the build height, with a) partially molten Ti-6Al-7Nb particles, b) small grains in areas of higher copper concentration with copper rich grain boundaries and c) larger grains in areas of lower copper concentration partially growing epitaxially indicating grain refinement with local columnar-to-equiaxed transition is caused by the copper addition.

Between the uppermost layers exhibiting dendritic solidification and β-grain refinement, some homogeneous layers are apparent. Based on LOM and EBSD, as well as on the broadening of the (1 0 -1 1) and (2 -1 -1 0) peaks, we propose the following mechanism taking place in 5Cu, 7Cu, and 9Cu: Following dendritic solidification and the dissolution of copper, α″ martensite forms, which subsequently transforms into a fine microstructure of α + β + Ti_2Cu as the temperature during reheating decreases sufficiently to allow the formation of the intermetallic phase. This process lowers the concentration of β-stabilising elements, thereby enabling the formation of α″. EDS measurements reveal significant elemental partitioning, with the β phase containing significant amounts of Cu in

 doi:10.20944/preprints202511.1915.v1

addition to Nb, which explains how retained β can coexist alongside α/α′. This proposed pathway is consistent with the observed microstructures, although the exact kinetics and the potential contribution of ultrafast diffusion or local segregation during PBF-LB/M remain subject to further investigation.

4.3. Mechanical Properties

Even though the employed in situ alloying strategy resulted in insufficient mixing, several insights regarding the mechanical properties and the influence of copper additions to Ti-6Al-7Nb can be drawn from the results. The observed increase in hardness with higher copper addition is attributed to a combination of solid solution strengthening, microstructural refinement, and precipitation hardening by finely dispersed Ti_2Cu particles. The inhomogeneous microstructure did not lead to a higher variation in hardness values. A possible compensatory mechanism in the copper-rich, softer or more brittle regions may be a locally higher content of intermetallic phases, enhanced precipitation hardening, and, overall, the inherently high hardness of intermetallic phases, e.g. microhardness of 700 HV5 reported for pure Ti_2Cu [43,44].

Subsequently, the brittleness of these phases likely accounts for the sharp decrease in elongation at break observed in tensile testing, which is accompanied by an increased presence of build defects such as liquation cracks and lack of fusion on the microscale; this conclusion is supported by the growing number of solidification cells seen on the fracture surfaces of samples with higher copper content. The cause of these microcracks and lack of fusion is probably the large difference in solidification temperature between Ti-6Al-7Nb and the eutectic point at approximately 65 wt.% Cu, exceeding 700 °C in equilibrium, and still more than 600 °C at 20 wt.% Cu. According to CALPHAD simulations, copper contents above 10 wt.% result in the formation of significant quantities of titanium aluminides. The proposed mechanism is that the formation of Ti_2Cu leads to local enrichment of aluminium, which in turn promotes the formation of titanium aluminides. EDS analysis of cleavage facets on fracture surfaces of 7Cu and 9Cu revealed aluminium concentrations above 20 at.%, indicating that the brittle fracture is caused by Ti_3Al formation, thus further highlighting the major role that insufficient mixing of Ti-6Al-7Nb and copper plays in the embrittlement observed during tensile testing.

5. Conclusions

This study investigated the in situ alloying of Ti-6Al-7Nb with varying copper contents (1 wt.% – 9 wt.%) via PBF-LB/M and systematically evaluated processability, microstructure, and mechanical properties. The main findings can be summarised as follows:

- High-density samples (> 99.9 %) were achieved for all compositions, but uniform copper distribution strongly depended on processing parameters, particularly energy density.
- Increasing copper content led to significant grain refinement and a columnar-to-equiaxed transition; however, inhomogeneities and copper segregation were observed at ≥ 5 wt.% Cu.
- XRD and SEM analyses revealed that copper additions promoted stabilisation of metastable β and precipitation of Ti_2Cu, with their fractions increasing with copper content.
- Hardness and yield strength increased nearly linearly with copper content due to solid solution strengthening, grain refinement, and precipitation hardening.
- Ductility decreased sharply beyond 5 wt.% Cu because brittle fracture mechanisms, hot cracking, and Ti_2Cu/Ti_3Al formation became dominant.
- Overall, moderate copper additions (≈ 1 wt.% – 3 wt.%) appear most promising, balancing mechanical performance and processability, while higher Cu levels lead to significant embrittlement and process-related defects.

Author Contributions: Conceptualization, P.S., K.-P.H. and M.S.; methodology, P.S., K.-P.H. and M.S.; validation, P.S., N.F.L.D., K.-P.H. and M.S.; formal analysis, P.S., K.-P.H. and M.S.; investigation, P.S., N.F.L.D. and R.Z.; resources, W.T. and M.S.; data curation, P.S.; writing—original draft preparation, P.S.; writing—review

 doi:10.20944/preprints202511.1915.v1

and editing, P.S., N.F.L.D., R.Z., K.-P.H., W.T. and M.S.; visualization, P.S.; supervision, K.-P.H., W.T. and M.S.; project administration, P.S.; funding acquisition, K.-P.H., W.T. and M.S. All authors have read and agreed to the published version of the manuscript.

Funding: This research was funded by the Deutsche Forschungsgemeinschaft (DFG, German Research Foundation) – grant numbers SCHA 1484/45-2 and TI 343/167-2 – project number 415285024.

Data Availability Statement: The data that support the findings of this study are available from the corresponding author upon reasonable request.

Acknowledgements: The author gratefully acknowledges the German Research Foundation (DFG) for the financial support. The research was performed with the equipment and base of the LWK and DMRC research infrastructure. The authors are grateful for the support provided by the LWK and DMRC staff members as well as to Dennis Milaege and Maxwell Hein for the valuable discussions.

Conflicts of Interest: The author declares no conflict of interest. The funders had no role in the design of the study; in the collection, analyses, or interpretation of data; in the writing of the manuscript, or in the decision to publish the results.

References

1. Kobayashi, E., Wang, T., Doi, H. et al. Mechanical properties and corrosion resistance of Ti–6Al–7Nb alloy dental castings. *Journal of Materials Science: Materials in Medicine* **9**, 567–574 (1998). https://doi.org/10.1023/A:1008909408948
2. Kobayashi, E.; Mochizuki, H.; Doi, H.; Yoneyama, T.; Hanawa, T. Fatigue Life Prediction of Biomedical Titanium Alloys under Tensile/Torsional Stress. Mater. Trans. **2006**, 47, pp. 1826–1831. https://doi.org/10.2320/matertrans.47.1826
3. Haase, F.; Siemers, C.; Klinge, L.; Lu, C.; Lang, P.; Lederer, S.; König, T.; Rösler, J. Aluminum- and Vanadium-free Titanium Alloys for Medical Applications. MATEC Web Conf. 2020, 321, 5008. https://doi.org/10.1051/matecconf/202032105008
4. Kim, K.T., Eo, M.Y., Nguyen, T.T.H. et al. General review of titanium toxicity. *Int J Implant Dent* **5**, 10 (2019). https://doi.org/10.1186/s40729-019-0162-x
5. Rojas-Lemus, M.; López-Valdez, N.; Bizarro-Nevares, P.; González-Villalva, A.; Ustarroz-Cano, M.; Zepeda-Rodríguez, A.; Pasos-Nájera, F.; García-Peláez, I.; Rivera-Fernández, N.; Fortoul, T.I. Toxic Effects of Inhaled Vanadium Attached to Particulate Matter: A Literature Review. *Int. J. Environ. Res. Public Health* **2021**, *18*, 8457. https://doi.org/10.3390/ijerph18168457
6. Chen, Q.; Thouas, G.A. Metallic implant biomaterials. Mater. Sci. Eng. R Rep. **2015**, 87, 1–57. https://doi.org/10.1016/j.mser.2014.10.001
7. Li, B.Q., Lu, X. A Biomedical Ti-35Nb-5Ta-7Zr Alloy Fabricated by Powder Metallurgy. J. of Materi Eng and Perform 28, 5616–5624 (2019). https://doi.org/10.1007/s11665-019-04294-7
8. Iijima, D.; Yoneyama, T.; Doi, H.; Hamanaka, H.; Kurosaki, N. Wear properties of Ti and Ti-6Al-7Nb castings for dental prostheses. Biomaterials **2003**, 24, 1519–1524. https://doi.org/10.1016/S0142-9612(02)00533-1
9. Guo, S.; Lu, Y.; Wu, S.; Liu, L.; He, M.; Zhao, C.; Gan, Y.; Lin, J.; Luo, J.; Xu, X.; Lin, J. Preliminary study on the corrosion resistance, antibacterial activity and cytotoxicity of selective-laser-melted Ti6Al4V-xCu alloys. Mater. Sci. Eng. C **2017**, 72, 631–640. https://doi.org/10.1016/j.msec.2016.11.126
10. Campoccia, D.; Montanaro, L.; Arciola, C.R. The significance of infection related to orthopedic devices and issues of antibiotic resistance. Biomaterials **2006**, 27, 2331–2339. https://doi.org/10.1016/j.biomaterials.2005.11.044
11. Zheng, Y.; Xu, X.; Xu, Z.; Wang, J.; Cai, H. Metallic Biomaterials: New Directions and Technologies; Wiley-VCH Verlag GmbH & Co. KGaA: Weinheim, Germany, **2017**.
12. Liu, J.; Li, F.; Liu, C.; Wang, H.; Ren, B.; Yang, K.; Zhang, E. Effect of Cu content on the antibacterial activity of titanium–copper sintered alloys. Mater. Sci. Eng. C **2014**, 35, 392–400. https://doi.org/10.1016/j.msec.2013.11.028

 doi:10.20944/preprints202511.1915.v1

13. Zhang, E.; Li, F.; Wang, H.; Liu, J.; Wang, C.; Li, M.; Yang, K. A new antibacterial titanium–copper sintered alloy: preparation and antibacterial property. Mater. Sci. Eng. C **2013**, 33, 4280–4287. https://doi.org/10.1016/j.msec.2013.06.016
14. Ma, Z.; Yao, M.; Liu, R.; Yang, K.; Ren, L.; Zhang, Y.; Liao, Z.; Liu, W.; Qi, M. Study on antibacterial activity and cytocompatibility of Ti–6Al–4V–5Cu alloy. Mater. Technol. **2015**, 30, B80–B85. https://doi.org/10.1016/j.msec.2013.11.028
15. Liu, R., Memarzadeh, K., Chang, B. et al. Antibacterial effect of copper-bearing titanium alloy (Ti-Cu) against Streptococcus mutans and Porphyromonas gingivalis. Sci Rep 6, 29985 (2016). https://doi.org/10.1038/srep29985
16. Song, Y.-H.; Kim, M.-K.; Park, E.-J.; Song, H.-J.; Anusavice, K.J.; Park, Y.-J. Cytotoxicity of alloying elements and experimental titanium alloys by WST-1 and agar overlay tests. Dent. Mater. 2014, 30, 977–983. https://doi.org/10.1016/j.dental.2014.05.012
17. Wang, X.; Dong, H.; Liu, J.; Qin, G.; Chen, D.; Zhang, E. In vivo antibacterial property of Ti-Cu sintered alloy implant. Mater. Sci. Eng. C 2019, 100, 38–47. https://doi.org/10.1016/j.msec.2019.02.084
18. Fowler, L.; Janson, O.; Engqvist, H.; Norgren, S.; Öhman-Mägi, C. Antibacterial investigation of titanium-copper alloys using luminescent Staphylococcus epidermidis in a direct contact test. Mater. Sci. Eng. C 2019, 97, 707–714. https://doi.org/10.1016/j.msec.2018.12.050
19. Alshammari, Y.; Yang, F.; Bolzoni, L. Low-cost powder metallurgy Ti-Cu alloys as a potential antibacterial material. J. Mech. Behav. Biomed. Mater. 2019, 95, 232–239. https://doi.org/10.1016/j.jmbbm.2019.04.004
20. Xu, X.; Lu, Y.; Li, S.; Guo, S.; He, M.; Luo, K.; Lin, J. Copper-modified Ti6Al4V alloy fabricated by selective laser melting with pro-angiogenic and anti-inflammatory properties for potential guided bone regeneration applications. Mater. Sci. Eng. C 2018, 90, 198–210. https://doi.org/10.1016/j.msec.2018.04.046
21. Krakhmalev, P.; Yadroitsev, I.; Yadroitsava, I.; de Smidt, O. Functionalization of biomedical Ti6Al4V via in situ alloying by Cu during laser powder bed fusion manufacturing. Materials 2017, 10, 1154. https://doi.org/10.3390/ma10101154
22. Williams, J.C., Taggart, R. & Polonis, D.H. The morphology and substructure of Ti-Cu martensite. *Metall Trans* **1**, 2265–2270 (1970). https://doi.org/10.1007/BF02643444
23. Donthula, H.; Vishwanadh, B.; Alam, T.; Borkar, T.; Contieri, R.J.; Caram, R.; Banerjee, R.; Tewari, R.; Dey, G.K.; Banerjee, S. Morphological evolution of transformation products and eutectoid transformation(s) in a hyper-eutectoid Ti-12 at% Cu alloy. Acta Mater. 2019, 168, 63–75. https://doi.org/10.1016/j.actamat.2019.01.044.
24. Dobromyslov, A.; Kazantseva, N. Phase transformations in the Ti-Cu system. Phys. Met. Metallogr. 2000, 89, 467–473.
25. Dobromyslov, A.V. Bainitic Transformations in Titanium Alloys. Phys. Metals Metallogr. 122, 237–265 (2021). https://doi.org/10.1134/S0031918X21030042
26. Takahashi, M.; Sato, K.; Togawa, G.; Takada, Y. Mechanical Properties of Ti-Nb-Cu Alloys for Dental Machining Applications. J. Funct. Biomater. 2022, 13, 263. https://doi.org/10.3390/jfb13040263
27. Zhao, Z.; Xu, W.; Xin, H.; Yu, F. Microstructure, corrosion and anti-bacterial investigation of novel Ti-xNb-yCu alloy for biomedical implant application. J. Mater. Res. Technol. 2022, 18, 5212–5225. https://doi.org/10.1016/j.jmrt.2022.04.158.
28. Li, Q.; Peng, Q.; Huang, Q.; Niinomi, M.; Ishimoto, T.; Nakano, T. Development and characterizations of low-modulus Ti–Nb–Cu alloys with enhanced antibacterial activities. Mater. Today Commun. 2024, 38, 108402. https://doi.org/10.1016/j.mtcomm.2024.108402.
29. Schmidt, M.; Merklein, M.; Bourell, D.; Dimitrov, D.; Hausotte, T.; Wegener, K.; Overmeyer, L.; Vollertsen, F.; Levy, G.N. Laser based additive manufacturing in industry and academia. CIRP Ann. 2017, 66, 561–583. https://doi.org/10.1016/j.cirp.2017.05.011
30. Nouri, A.; Rohani Shirvan, A.; Li, Y.; Wen, C. Additive manufacturing of metallic and polymeric load-bearing biomaterials using laser powder bed fusion: A review. J. Mater. Sci. Technol. 2021, 94, 196–215. https://doi.org/10.1016/j.jmst.2021.03.058

31. Gatto, M.L.; Furlani, M.; Giuliani, A.; Bloise, N.; Fassina, L.; Visai, L.; Mengucci, P. Biomechanical performances of PCL/HA micro- and macro-porous lattice scaffolds fabricated via laser powder bed fusion for bone tissue engineering. Mater. Sci. Eng. C 2021, 128, 112300. https://doi.org/10.1016/j.msec.2021.112300
32. Wu, J.; Wang, X.Q.; Wang, W.; Attallah, M.M.; Loretto, M.H. Microstructure and strength of selectively laser melted AlSi10Mg. Acta Mater. 2016, 117, 311–320. https://doi.org/10.1016/j.actamat.2016.07.012
33. Oliveira, J.P.; LaLonde, A.D.; Ma, J. Processing parameters in laser powder bed fusion metal additive manufacturing. Mater. Des. 2020, 193, 108762. https://doi.org/10.1016/j.matdes.2020.108762
34. Shaikh, A.; Kumar, S.; Dawari, A.; Kirwai, S.; Patil, A.; Singh, R. Effect of temperature and cooling rates on the α+β morphology of Ti-6Al-4V alloy. Procedia Struct. Integr. 2019, 14, 782–789. https://doi.org/10.1016/j.prostr.2019.07.056
35. Liu, S.; Shin, Y.C. Additive manufacturing of Ti6Al4V alloy: A review. Mater. Des. 2019, 164, 107552. https://doi.org/10.1016/j.matdes.2018.107552
36. Kok, Y.; Tan, X.P.; Wang, P.; Nai, M.; Loh, N.H.; Liu, E.; Tor, S.B. Anisotropy and heterogeneity of microstructure and mechanical properties in metal additive manufacturing: A critical review. Mater. Des. 2018, 139, 565–586. https://doi.org/10.1016/j.matdes.2017.11.021
37. Mahmud, A.; Huynh, T.; Zhou, L.; Hyer, H.; Mehta, A.; Imholte, D.D.; Woolstenhulme, N.E.; Wachs, D.M.; Sohn, Y. Mechanical Behavior Assessment of Ti-6Al-4V ELI Alloy Produced by Laser Powder Bed Fusion. Metals 2021, 11, 1671. https://doi.org/10.3390/met11111671
38. Chlebus, E.; Kuźnicka, B.; Kurzynowski, T.; Dybała, B. Microstructure and mechanical behaviour of Ti–6Al–7Nb alloy produced by selective laser melting. Mater. Charact. 2011, 62, 488–495. https://doi.org/10.1016/j.matchar.2011.03.006.
39. Hein, M.; Hoyer, K.-P.; Schaper, M. Additively processed TiAl6Nb7 alloy for biomedical applications. Mater. Werkst. 2021, 52, 703–716. https://doi.org/10.1002/mawe.202000288
40. Milaege, D.; Eschemann, N.; Hoyer, K.-P.; Schaper, M. Anisotropic Mechanical and Microstructural Properties of a Ti-6Al-7Nb Alloy for Biomedical Applications Manufactured via Laser Powder Bed Fusion. *Crystals* **2024**, *14*, 117. https://doi.org/10.3390/cryst14020117.
41. Gargalis, L.; Ye, J.; Strantza, M.; Rubenchik, A.; Murray, J.W.; Clare, A.T.; Ashcroft, I.A.; Hague, R.; Matthews, M.J. Determining processing behaviour of pure Cu in laser powder bed fusion using direct micro-calorimetry. J. Mater. Process. Technol. 2021, 294, 117130. https://doi.org/10.1016/j.jmatprotec.2021.117130.
42. Zhang, D., Qiu, D., Gibson, M.A. et al. Additive manufacturing of ultrafine-grained high-strength titanium alloys. Nature 576, 91–95 (2019). https://doi.org/10.1038/s41586-019-1783-1.
43. Fan, Y.; Fan, J.; Wang, C. Formation of typical Cu–Ti intermetallic phases via a liquid-solid reaction approach. Intermetallics 2019, 113, 106577. https://doi.org/10.1016/j.intermet.2019.106577.
44. Akbarpour, M.R.; Alikhani Hesari, F. Synthesis of copper nanoparticles by electrochemical reduction: The effect of the preparation conditions on the particle size. Mater. Res. Express 2016, 3, 045004. https://doi.org/10.1088/2053-1591/3/4/045004.